Macroscale Control of Reactivity using 3D Printed Materials with Intrinsic Catalytic Properties

J. Sebastián Manzano,[a,b] Hsin Wang,[a,b] Long Qi[a] and Igor I. Slowing[a,b]*

[a]*US DOE Ames Laboratory, Ames, Iowa 50011, United States*
[b]*Department of Chemistry, Iowa State University, Ames, Iowa 50011, United States*
E-mail: islowing@iastate.edu

Keywords: 3D printing, heterogeneous catalysis, macroscale topology, hydrolysis, reactive surfaces

Abstract

The morphology of heterogeneous catalysts can impact their performance by controlling the efficiency of heat and mass transfer. However, standard manufacturing methods such as extrusion or pelleting offer little options for optimizing catalyst shape. Herein, stereolithographic (SLA) 3D printing is used to directly produce catalysts with controlled morphologies to enhance their performance. A series of chemically active magnetic stir-bar compartments (SBC) were 3D printed and used as catalysts for sucrose hydrolysis. The SBCs were composed of acrylic acid (AA) and 1,6-hexanediol diacrylate (HDDA) which provided acid sites and hydrophobic crosslinking domains, respectively. Fixing the surface area and the number of accessible catalytic sites of the 3D printed SBC allowed exploring the effect of changes in morphology on the fluid dynamics of the reaction systems, and consequently on the efficiency of the catalytic hydrolysis. Moreover, varying the AA:HDDA ratios in SBC allowed tuning the surface-substrate interaction to control their catalytic activity for the hydrolysis of sucrose. This work demonstrates that 3D printing catalytic materials enable optimizing catalyst performance by simultaneously controlling macroscopic and molecular properties.

1. Introduction

The macroscopic structure of solid catalysts can affect the efficiency of heat and mass transfer in chemical conversions.[1-5] Solid catalysts are typically manufactured by pelleting or extruding composites of pre-catalysts, promoters and binders.[6-10] Although these methods can yield different catalyst shapes like grids, beads, rods or foams, these topologies are not necessarily optimal for all types of reactor and process.[11-16] Unfortunately, standard manufacturing methods can hardly go beyond these very simple shapes.[9] This limitation hinders the development and adoption of structures that could further enhance catalyst performance by influencing reactant flow dynamics.

3D printing is a manufacturing technique that uses digital designs to assemble materials layer by layer. This technology has been recently applied to the production of biomaterials,[17-20] electrochemical devices,[21, 22] microfluidic devices,[23-27] ceramics,[28-35] and catalysts.[28, 29, 36, 37] In catalytic applications, active sites can be integrated into the architectures either during or after 3D printing. While the direct printing approach may be desirable for its simplicity, it often requires post-printing treatments such as etching to expose buried sites or sintering to improve mechanical resistance. However, these additional steps usually alter the structure of the surface, defeating in part the purpose of 3D printing and complicating the overall process.

We have recently introduced a method to directly 3D print active catalysts that does not require severe post-printing treatments.[36] The approach is based on stereolithography (SLA) of substituted olefins. This method enables the direct manufacturing of bespoke devices (e.g. millifluidic reactors, UV-Vis reactive adaptors) with customizable catalytic properties (e.g. acidic, basic, metallic). Herein we applied this method to 3D print a set of structures with acidic active sites and explored the effects of topology, surface area, and chemical composition on their catalytic performance for the hydrolysis of sucrose. The 3D

design consisted of a magnetic stir-bar compartment (SBC) attached to rotors with curved blades (Figure 1). We devised the materials to expose hydrophobic domains and acid catalytic sites by using 1,6-hexanediol diacrylate (HDDA) and acrylic acid (AA) as cross-linker and monomer respectively. The SBC were then used to investigate the effects of molecular composition on the catalytic performance of the SBC.

2. Experimental Section

2.1. *Materials:* Acrylic acid (AA), 1,6-hexanediol diacrylate (HDDA), poly(ethylene glycol) diacrylate Mn 575 (PEGDA), phenylbis(2,4,6-trimethylbenzoyl)phosphine oxide (BAPO), p-anisaldehyde dimethyl acetal, anhydrous sodium carbonate and potassium thiocyanate were purchased from Sigma-Aldrich (St. Louis, MO, USA). Sodium citrate, copper(II)sulfate and sucrose were purchased from Fischer Scientific (Waltham, MA, USA). Potassium ferricyanide was purchased from EM Science (Darmstadt, Germany). All reagents were used without any further purification.

2.2. *Catalytic resin:* Acrylic acid (7 mL, 102 mmol) was mixed with PEGDA (3 mL, 5.8 mmol) in an Amber flask. Then, BAPO (0.100 g, 0.24 mmol) was added to the resin and the mixture was sonicated for 1 min. The solution was poured into the resin tank of a FormLabs Form 1+^{TM} 3D printer (Somerville, MA, USA) and used for printing. The settings used were: *laser power*: 62 mW, *first layer passes*: 10, *other layer passes*: 4, and *early layer passes*: 5.

2.3. *Water tolerant catalytic resin:* Acrylic acid (7.3, 14.6, 29.1, 43.7, 72.9 or 102 mmol) was mixed with 1,6-hexanedioldiacrylate (HDDA) (31, 220 or 130 mmol) in an Amber flask. Then BAPO (0.100 g, 0.24 mmol) was added to the resin and the mixture was sonicated for 1 min. The solution was poured into the resin tank of a FormLabs Form 1+^{TM} 3D printer

(Somerville, MA, USA) and used for printing. The settings used were: *laser power*: 62 mW, *first layer passes*: 10, *other layer passes*: 4, and *early layer passes*: 5.

2.4. *3D printing:* The CAD designs were prepared using AutoCad 2019 software and exported as STL files (Supplementary files available). A FormLabs Form 1+^{TM} 3D printer (405 nm laser) was used for the laser polymerization. After printing, the unreacted monomer was removed from the printed objects by immersion in an acetone bath for 1 h. Final curing was performed by exposing the 3D object to UV irradiation (λ = 320 nm) in a Rayonet photoreactor for 10 min.

2.5. *Active sites estimation:* The 3D-printed impellers were immersed in 5 mL of deionized water (18 MΩ). The pH was measured with an Accumet benchtop pH meter at 20 °C. Equation 1 was used to estimate the number of accessible sites:

$$Active\ sites\ (\mu mol\ g^{-1}) = \frac{(\frac{[H^+]^2+K_a[H^+]}{K_a}-[H^+_{water}])\times V}{m_{SBC}} \qquad \text{(S1)}$$

were $[H^+]$ is the concentration of protons (μM) in the solution containing the 3D printed SBC, K_a is the equilibrium constant for polyacrylic acid (6.31×10^{-5}), $[H^+_{water}]$ is the concentration of protons in the reference sample (μM, no 3D printed SBC), *V* is the volume of the solution in L, and m_{SBC} is the mass of SBC in g.

2.6. *Solvent compatibility assays:* 3D printed impellers were immersed in 5 mL of water inside a closed 20 mL vial. The vial was set in a heated aluminum block and stirred at 500 rpm for 24 h at 65 °C. Then, the 3D printed impellers were visually examined, and the supernatants were tested for residues of polymer by ESI-MS on an Agilent QTOF 6540.

Attenuated Total Reflectance Fourier Transform Infrared (ATR-FTIR) Spectroscopy: Measurements were made on a Bruker Vertex 80 FT-IR spectrometer with OPUS software. The spectrometer was equipped with a diamond sealed high pressure clamp ATR MIRacle PIKE accessory where the 3D-printed samples were pressed against the crystal to collect the

respective spectrum. 32 scans were collected for each measurement in absorbance mode with 4 cm^{-1} resolution.

2.7. *Sucrose hydrolysis reaction***:** Sucrose (130 mg, 0.38 mmol) was dissolved in 1 mL of water. Then, a 3D printed impeller was added to the mixture. The solution was placed in an aluminum block and stirred at 500 rpm at 65 °C for 3 h. An aliquot of the reaction mixture (10 µL) was added to 1 mL of water, and the dilution was analyzed on a Waters ACQUITY H-Class UPLC system equipped with a single-quadrupole mass detector (ACQUITY QDa). The analysis were also performed with Waters Process Analysis UPLC Systems (ACQUITY Patrol) with refractive index detector operated at 40 °C. Reactants and products were separated using a Waters ACQUITY UPLC BEH Amide Column (130Å, 1.7 µm, 2.1 mm × 150 mm) at 40 °C using acetonitrile:water mixture (80:20 v:v, with 0.1% NH_4OH) as the mobile phase at a flow rate of 0.5 mL min^{-1}. Catalytic performance parameters were calculated according to equations S2 and S3. The amounts of active sites were obtained by weighting the SBC and applying equation S1.

$$\%Conversion = \frac{mmol_{gluocse,fructose}}{mmol_{sucrose_0}} \times 100 \qquad \text{(S2)}$$

$$TON = \frac{mmol_{gluocse+fructose}}{mmol_{active\ sites}} \qquad \text{(S3)}$$

2.8. *Computational fluidic dynamic (CFD) simulations:* Simulations of the mixing process were done in CFD using an ANSYS™ Fluent 18.1 solver. The simulations were performed using the pressure-based steady state velocity conditions with gravity acting in the negative z-axis direction. The fluid regions were set to viscous type in the k-ε standard model with scalable wall functions. The material was chosen as water-liquid. The movement of the impeller zone in the tank-fluid region was modeled using a Multiple Reference Frame (MRF) approach. The moving zone consisted of the impeller rotating with an angular velocity of 500 rpm along the z-axis. For the simulation a Hybrid initialization technique was used before

running the calculations with 1000 iterations. Velocity and pressure profiles were generated in CFD-post process to represent the effects of each SBC.

2.9. *Fluorescence microscopy:* A set of 8 × 8 × 1 mm slabs were 3D printed using resins having 5, 10, 20, 30, 40, 50, 60 and 70 volume % AA. The slabs were immersed for 10 min in a solution of Nile Red in acetone (1 mL, 0.1 m/v %) in an orbital shaker at 200 rpm. The samples were then removed from the solution, rinsed once with fresh acetone and analyzed by fluorescence microscopy in a Carl Zeiss Axioskop 40 FL with a HBO 50 fluorescent illuminator at 40× magnification using a BP546/12 LP590 filter. The fluorescence intensities of the micrographs were quantified using ImageJ software all values were normalized relative to the highest intensity sample.

3. Results and discussion

Our first generation of photo-curable resin used acrylic acid (AA) as monomer and source of acidic sites, and poly(ethylene glycol) diacrylate (PEGDA) as crosslinker.[36] However, the 3D printed materials prepared from this resin could only be used in organic solvents because they degraded when vigorously shaken in water due to the highly hydrophilic nature of PEGDA. To overcome this limitation, we developed a second generation photo-curable resin using the more hydrophobic 1,6-hexanediol diacrylate (HDDA) as crosslinker.[38] Immersion of the HDDA crosslinked SBC in water and stirring at 500 rpm and 65 °C for 24 h gave no appreciable degradation of the material (**Figure S1a** and **b**). ESI-MS analysis of the supernatant did not show any monomer or oligomer peaks (**Figure S2a**). In contrast, the objects 3D printed using PEGDA as crosslinker were severely damaged upon stirring in water under the same conditions (**Figure S1c and d**). ESI-MS spectrum of the supernatant showed characteristic oligomer peaks with m/z 44.02 assigned to the ethyleneoxy repeating units of PEGDA, confirming degradation of the 3D printed object (**Figure S2b**).

The active site accessibility of the HDDA-crosslinked structures was evidenced by immersion in aqueous copper (II) nitrate.[36] A cross section of the reacted solid revealed formation of a copper-containing layer ca. 50 μm deep (**Figure S3**), indicating the non-porous nature of the 3D printed material.[36]

To evaluate the effects of macrostructure and surface on catalytic performance we used the AA/HDDA resin to 3D print a set of SBC with varying number of blades (2, 4 and 6) of the same size and curvature. The structures were designated as SBC-X where X represents the number of blades (**Figure 1**). Considering the final architecture is non-porous, the number of active sites cannot be estimated based solely on resin composition and mass. Thus, the amount of accessible catalytic sites in the 3D printed SBC were estimated by immersing them in water, measuring the pH and applying the pK_a of poly(acrylic acid) to the equilibrium expression (**Equation S1**).[36] The amounts of active sites were proportional to the calculated surface areas of the SBC (**Table S1**). This result suggested a homogeneous dispersion of active sites in the 3D printed objects regardless of their shape. To study the effects of macroscopic morphology on reactivity we used the SBC as catalysts for the acid hydrolysis of sucrose to D-glucose and D-fructose. This reaction is commonly used as a model of polysaccharide deconstruction and proceeds through initial protonation of the glycosidic oxygen followed by slow decomposition of the intermediate (**Scheme 1**).[39, 40] Surprisingly, in spite of the differences in the amount of sites sucrose conversion was very similar using SBC-2 and SBC-6, but slightly lower using SBC-4 as catalyst (**Figure S4**). Normalizing conversions by the number of active sites in the SBC (turnover number, TON), revealed a drop in activity with increasing number of blades (**Figure 2**). This result, although counterintuitive, indicates that the catalytic performance of SBC does not depend exclusively on the number of accessible active sites, but the shape/morphology of the SBC is playing an important role during the reaction. The surface topology of the rotating SBC should be able

to tune the interactions between the substrate and catalytic sites, all determined by the flow dynamics of the system.

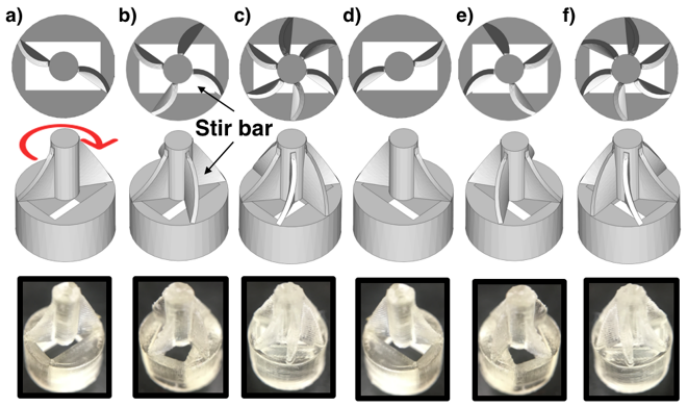

Figure 1. Top- and side-views of CAD models and photographs of 3D printed magnetic-stir-bar compartments (SBC). A 3 x 5 mm magnetic stir bar fits in the rectangular cavity in the base of the SBC. a) SBC-2, b) SBC-4, c) SBC-6, d) SBC-2R, e) SBC-4R, and f) SBC-6R. The direction of rotation is the same for all SBC and is indicated by the curved arrow.

To further investigate the effect of flow dynamics on apparent catalytic activity, we reversed the orientation of the blades in SBC. The new prints were designated as SBC-X-R, and were mirror images of the original SBC. Interestingly, in spite of having the same surface areas and similar number of active sites, all SBC-X-R consistently displayed higher activities than the corresponding SBC-X (**Figure 2** and **Table S1**). This result confirmed that macroscale topology plays an important role on catalyst performance. Importantly, executing the catalytic reaction at different stir rates (100, 500 and 1000 rpm) did not give significant variations in conversion, indicating that the observed behavior was not due to mass transfer limitations (**Figure S5**).

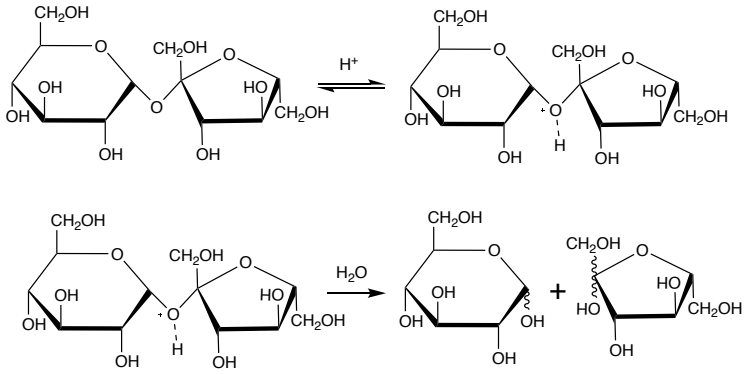

Scheme 1. Acid catalyzed hydrolysis of sucrose.

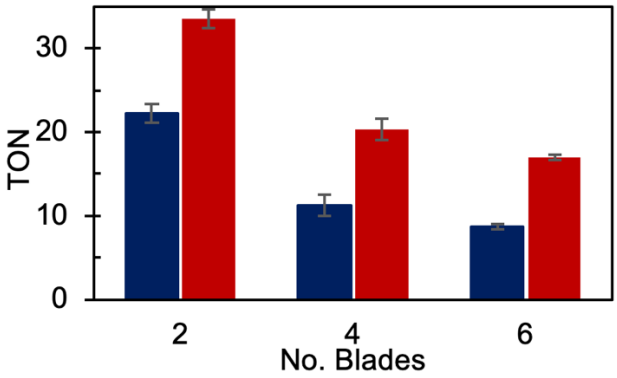

Figure 2. Turnover numbers (TON) of 3D printed SBC-X (blue) and their corresponding SBC-X-R (red) for the hydrolysis of sucrose. Conditions: one SBC, 0.38 M sucrose in water (1 mL), 500 rpm, 65 °C, 3 h.

Flow dynamics can affect the activities of heterogeneous catalysts by controlling the number of effective contacts between the reactants in solution and the active sites on the catalytic surfaces. Because of the blades twist direction relative to the magnetic stir bar rotation, the SBC-X push the liquid away from their rotation axes, while the SBC-X-R pull the liquid towards their axes (**Figure S6**). This difference was evidenced by following the dispersion of methylene blue in water stirred with SBC-4 and SBC-4-R. Photographs of early stages of mixing revealed that SBC-4-R formed a narrow funnel and concentrated initially the dye in the lower portion of the vial. In contrast, SBC-4 appeared to spread the dye faster throughout the whole container (**Figure S7**). Pressure contour maps generated by computational fluid dynamics (CFD) simulations provided insights about the substrate-surface

interactions in the SBC systems (**Figure 3, S8** and **S9**). The simulations indicated that the percent of non-zero pressure areas on the SBC surface decreases with increasing number of blades, and is higher for SBC-X-R than for their corresponding SBC-X (**Figure 3, S8,** and **S9**). This behavior correlates with the observed differences in catalytic performance (**Figure S10**), and may therefore be an indicator of the number of effective contacts between the reactants and the catalytic surface of SBC.

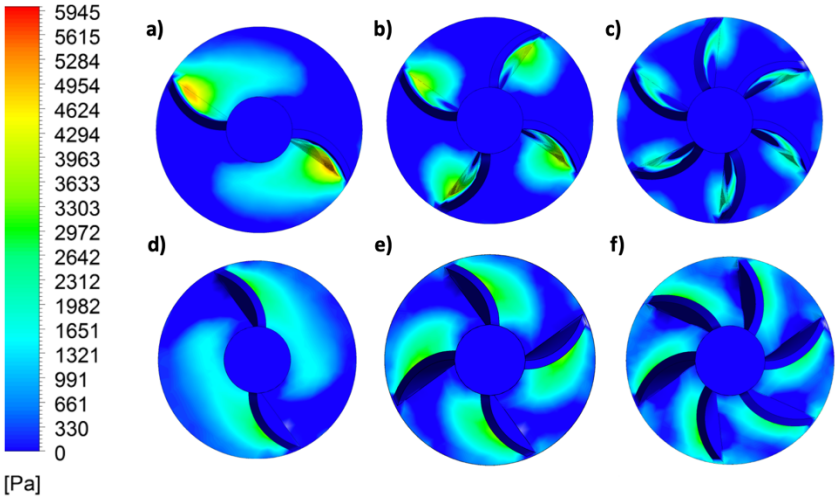

Figure 3. Top view of pressure contour maps of a) SBC-2, b) SBC-4, c) SBC-6, d) SBC-2-R, e) SBC-4-R and f) SBC-6-R. Left: pressure scale in Pa.

Monosaccharides are a common feedstock in biorefinery and are typically produced by enzymatic hydrolysis of complex sugars.[41-44] To break down polysaccharides, enzymes use hydrophobic domains that bind the substrates via van der Waals interactions. This binding assumes most of the entropic cost of activation and thereby facilitates glycosidic bond cleavage by weakly acidic active sites.[45] A similar type of synergy seems to occur in the activated-carbon catalyzed deconstruction of cellulose: the hydrophobic surface of the material enables even weakly acidic phenols to promote the hydrolysis.[46-49] Based on this information, we decided to explore the effect of varying the amounts of hydrophobic HDDA crosslinker on the catalytic performance of 3D printed SBC for the hydrolysis of sucrose. To this end, we prepared a series of precursor resins with varying AA:HDDA ratios and printed a

set of SBC-6-R. The materials were designated as SBC-6-R-*n*, where *n* corresponded to the volume percent of AA used in the original composition (5, 10, 20, 30, 40, 50, 60 and 70 %). The 3D printed SBC-6-R-*n* did not show any obvious variations in texture, mechanical strength or print resolution (**Figure S11**). ATR FTIR analysis of the SBC-6-R-*n* showed a red-shift in the carbonyl band with increasing AA:HDDA mole ratios, consistent with an increase of carboxylic acid moieties on the surface of the 3D printed objects (**Figure S12**). The C=O band was deconvoluted into two peaks centered at 1700 and 1730 cm^{-1} characteristic of hydrogen bonded carboxylic acids in polyacrylic acid, and ester carbonyls of HDDA, respectively (**Figure S13 and Table S2**).[50, 51] The peak areas correlated well with the mole ratios of the precursors in the resins, and provided a measure of the proportion of hydrophobic domains relative to the acidic sites in the SBC-6-R-*n*. The hydrophobicity of the materials was examined by immersing them in a Nile Red solution. The fluorescence of Nile Red increases with decreasing polarity of its environment.[52, 53] Fluorescence microscopy analysis confirmed the homogenous distribution of the hydrophobic groups adsorbed on the surface of the SBC-6-R-*n* (**Figure S14**). Furthermore, the intensity of the fluorescence emission decreased with increasing proportion of AA in the 3D printed polymers (**Figure S15**).

The SBC-6-R-*n* were then evaluated as catalysts for the hydrolysis of sucrose. As expected, sucrose conversion increased with the amount of accessible active sites in the SBC-6-R-*n*. Interestingly however, sucrose conversion displayed a sigmoidal-like dependence on the AA:HDDA ratios of the materials (**Figure 4**), which may suggest cooperativity between the two components of the material.[54-58] The results indicated that increasing the density of acidic sites (AA) led to large enhancements in conversion only when the ratio between active sites to hydrophobic domains (AA:HDDA) was between 1.6 and 3 (slope of this segment in Figure 4 was 9.7). Conversely, varying AA:HDDA ratios in the 0 – 1.6 or >3 regimes had

smaller effects on conversion (slopes of 4.1 and 0.3, respectively). This indicates that sucrose hydrolysis is facilitated by achieving an optimal balance between acidic and hydrophobic domains on the SBC surface. The results suggest a synergy between glycosidic bond activation by acidic AA sites and sucrose binding to the surface.

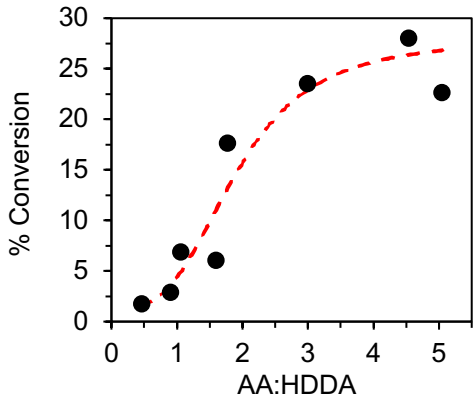

Figure 4. Dependence of sucrose conversion on AA:HDDA ratios of SBC-6-R.

4. Conclusions

In summary, this work demonstrated the simultaneous control of physical, topological and chemical properties of 3D printed materials. First, the nature of cross-linkers determines solvent compatibility of the 3D printed materials: while hydrophilic poly(ethyleneglycol)-based crosslinkers degraded in presence of water, hydrophobic HDDA cross-linkers gave water-tolerant architectures. Second, the topology of the 3D printed SBC controlled the flow dynamics of the reaction systems and led to variations in their catalytic efficiencies for sucrose hydrolysis. These variations were attributed to differences in the effective contact areas between the reactants and the catalytic surfaces. The results prove that small yet precise changes in the shape of the 3D printed objects, easily accessible with our methodology, can have dramatic effects on catalyst performance. Finally, our 3D printing method also allowed controlling the molecular composition of the catalytic architectures to tune and favor interactions between active sites and hydrophobic domains. Importantly, this new approach for 3D printing active materials offers control of catalytic properties all the way from the

molecular to the macroscale, which enables their application to advanced tasks in heterogeneous catalysis.

Acknowledgements

This research is supported by the U.S. Department of Energy, Office of Basic Energy Sciences, Division of Chemical Sciences, Geosciences, and Biosciences through Ames Laboratory. Ames Laboratory is operated for the U.S. Department of Energy by Iowa State University under Contract No. DE-AC02-07CH11358.

References

[1] G.C. Bond, K.S.W. Sing, D.H. Everett, R.A.W. Haul, L. Moscou, R.A. Pierotti, J. Rouquerol, T. Siemieniewska, Annexes, Handbook of Heterogeneous Catalysis, Wiley-VCH2008, pp. 1489-1588.
[2] J.F. LePage, R. Schlögl, M.S. Wainwright, F. Schü, K. Unger, E.I. Ko, H. Jacobsen, P. Kleinschmit, R.G. Menon, B. Delmon, K.Y. Lee, M. Misino, S.T. Oyama, Preparation of Solid Catalysts: Sections 2.0 and 2.1, Handbook of Heterogeneous Catalysis, Wiley-VCH2008, pp. 49-138.
[3] D.L. Johnson, X.E. Verykios, Effects of radially nonuniform distributions of catalytic activity on performance of spherical catalyst pellets, AIChE J. 30 (1984) 44-50.
[4] P.T. bai, V. Manokaran, P.S. Saiprasad, S. Srinath, Studies on Heat and Mass Transfer Limitations in Oxidative Dehydrogenation of Ethane Over Cr2O3 /Al2O3 Catalyst, Proc. Eng. 127 (2015) 1338-1345.
[5] F. Hibbe, J. Caro, C. Chmelik, A. Huang, T. Kirchner, D. Ruthven, R. Valiullin, J. Kärger, Monitoring Molecular Mass Transfer in Cation-Free Nanoporous Host Crystals of Type AlPO-LTA, J. Am. Chem. Soc. 134 (2012) 7725-7732.
[6] W.M.H. Sachtler, G. Schulz-Ekloff, S. Ernst, J.J. Friplat, K. Tanabe, H. Hattori, J.F. Le Page, M. Baerns, E. Körting, Preparation of Solid Catalysts: Sections 2.3.4 – 2.6, Handbook of Heterogeneous Catalysis, Wiley-VCH2008, pp. 365-426.
[7] V.G. Baldovino-Medrano, M.T. Le, I. Van Driessche, E. Bruneel, C. Alcázar, M.T. Colomer, R. Moreno, A. Florencie, B. Farin, E.M. Gaigneaux, Role of shaping in the preparation of heterogeneous catalysts: Tableting and slip-casting of oxidation catalysts, Catal. Today 246 (2015) 81-91.
[8] S.Y. Devyatkov, A.A. Zinnurova, A. Aho, D. Kronlund, J. Peltonen, N.V. Kuzichkin, N.V. Lisitsyn, D.Y. Murzin, Shaping of Sulfated Zirconia Catalysts by Extrusion: Understanding the Role of Binders, Ind. Eng. Chem. Res. 55 (2016) 6595-6606.
[9] J. Hagen, Catalyst Shapes and Production of Heterogeneous Catalysts, in: Wiley-VCH (Ed.) Industrial Catalysis2015, pp. 211-238.
[10] Y.Y. Li, S.P. Perera, B.D. Crittenden, J. Bridgwater, The effect of the binder on the manufacture of a 5A zeolite monolith, Powder Technol. 116 (2001) 85-96.

[11] J.T. Richardson, D. Remue, J.K. Hung, Properties of ceramic foam catalyst supports: mass and heat transfer, Appl. Catal. A 250 (2003) 319-329.
[12] Y. Liu, S. Podila, D.L. Nguyen, D. Edouard, P. Nguyen, C. Pham, M.J. Ledoux, C. Pham-Huu, Methanol dehydration to dimethyl ether in a platelet milli-reactor filled with H-ZSM5/SiC foam catalyst, Appl. Catal. A 409-410 (2011) 113-121.
[13] G. Incera Garrido, F.C. Patcas, S. Lang, B. Kraushaar-Czarnetzki, Mass transfer and pressure drop in ceramic foams: A description for different pore sizes and porosities, Chem. Eng. Sci. 63 (2008) 5202-5217.
[14] M. Lacroix, P. Nguyen, D. Schweich, C. Pham Huu, S. Savin-Poncet, D. Edouard, Pressure drop measurements and modeling on SiC foams, Chem. Eng. Sci. 62 (2007) 3259-3267.
[15] F.C. Patcas, G.I. Garrido, B. Kraushaar-Czarnetzki, CO oxidation over structured carriers: A comparison of ceramic foams, honeycombs and beads, Chem. Eng. Sci. 62 (2007) 3984-3990.
[16] T. Ludwig, J. Seckendorff, C. Troll, R. Fischer, M. Tonigold, B. Rieger, O. Hinrichsen, Additive Manufacturing of Al2O3‐Based Carriers for Heterogeneous Catalysis, Chem. Ing. Tech. 90 (2018) 703-707.
[17] R.A. Barry, R.F. Shepherd, J.N. Hanson, R.G. Nuzzo, P. Wiltzius, J.A. Lewis, Direct-Write Assembly of 3D Hydrogel Scaffolds for Guided Cell Growth, Adv. Mater. 21 (2009) 2407-2410.
[18] T. Boland, T. Xu, B. Damon, X. Cui, Application of inkjet printing to tissue engineering, Biotechnol. J. 1 (2006) 910-917.
[19] S. Mohanty, L.B. Larsen, J. Trifol, P. Szabo, H.V.R. Burri, C. Canali, M. Dufva, J. Emnéus, A. Wolff, Fabrication of scalable and structured tissue engineering scaffolds using water dissolvable sacrificial 3D printed moulds, Mater. Sci. Eng.: C 55 (2015) 569-578.
[20] C.N. Kelly, A.T. Miller, S.J. Hollister, R.E. Guldberg, K. Gall, Design and Structure–Function Characterization of 3D Printed Synthetic Porous Biomaterials for Tissue Engineering, Adv. Healthcare Mater. 7 (2018) 1701095.
[21] B.Y. Ahn, E.B. Duoss, M.J. Motala, X. Guo, S.-I. Park, Y. Xiong, J. Yoon, R.G. Nuzzo, J.A. Rogers, J.A. Lewis, Omnidirectional Printing of Flexible, Stretchable, and Spanning Silver Microelectrodes, Science 323 (2009) 1590-1593.
[22] B. Zhang, S. Li, H. Hingorani, A. Serjouei, L. Larush, A.A. Pawar, W.H. Goh, A.H. Sakhaei, M. Hashimoto, K. Kowsari, S. Magdassi, Q. Ge, Highly stretchable hydrogels for UV curing based high-resolution multimaterial 3D printing, J. Mater. Chem. B 6 (2018) 3246-3253.
[23] M. Alizadehgiashi, A. Gevorkian, M. Tebbe, M. Seo, E. Prince, E. Kumacheva, 3D-Printed Microfluidic Devices for Materials Science, Adv. Mater. Technol. 3 (2018) 1800068.
[24] V. Dragone, V. Sans, M.H. Rosnes, P.J. Kitson, L. Cronin, 3D-printed devices for continuous-flow organic chemistry, Beilstein J. Org. Chem. 9 (2013) 951−959
[25] P.J. Kitson, M.H. Rosnes, V. Sans, V. Dragone, L. Cronin, Configurable 3D-Printed millifluidic and microfluidic 'lab on a chip' reactionware devices, Lab on a Chip 12 (2012) 3267-3271.
[26] W. Lee, D. Kwon, W. Choi, G.Y. Jung, S. Jeon, 3D-Printed Microfluidic Device for the Detection of Pathogenic Bacteria Using Size-based Separation in Helical Channel with Trapezoid Cross-Section, Sci. Rep. 5 (2015) 7717.
[27] A.K. Au, W. Huynh, L.F. Horowitz, A. Folch, 3D-Printed Microfluidics, Angew. Chem. Int. Ed. 55 (2016) 3862-3881.
[28] A.S. Díaz-Marta, C.R. Tubío, C. Carbajales, C. Fernández, L. Escalante, E. Sotelo, F. Guitián, V.L. Barrio, A. Gil, A. Coelho, Three-Dimensional Printing in Catalysis: Combining

3D Heterogeneous Copper and Palladium Catalysts for Multicatalytic Multicomponent Reactions, ACS Catal. 8 (2018) 392-404.
[29] C.R. Tubío, J. Azuaje, L. Escalante, A. Coelho, F. Guitián, E. Sotelo, A. Gil, 3D printing of a heterogeneous copper-based catalyst, J. Catal. 334 (2016) 110-115.
[30] C.R. Tubío, F. Guitián, A. Gil, Fabrication of ZnO periodic structures by 3D printing, J. Eur. Ceram. Soc. 36 (2016) 3409-3415.
[31] J.A. Lewis, Colloidal Processing of Ceramics, J J. Am. Ceram. Soc 83 (2000) 2341-2359.
[32] B.G. Compton, J.A. Lewis, 3D-Printing of Lightweight Cellular Composites, Adv. Mater. 26 (2014) 5930-5935.
[33] R.B. Rao, K.L. Krafcik, A.M. Morales, J.A. Lewis, Microfabricated Deposition Nozzles for Direct-Write Assembly of Three-Dimensional Periodic Structures, Adv. Mater. 17 (2005) 289-293.
[34] G. Varghese, M. Moral, M. Castro-García, J.J. López-López, J.R. Marín-Rueda, V. Yagüe-Alcaraz, L. Hernández-Afonso, J.C. Ruiz-Morales, J. Canales-Vázquez, Fabrication and characterisation of ceramics via low-cost DLP 3D printing, Bol. Soc. Esp. Ceram. Vidrio 57 (2018) 9-18.
[35] F. Kotz, K. Arnold, W. Bauer, D. Schild, N. Keller, K. Sachsenheimer, T.M. Nargang, C. Richter, D. Helmer, B.E. Rapp, Three-dimensional printing of transparent fused silica glass, Nature 544 (2017) 337.
[36] J.S. Manzano, Z.B. Weinstein, A.D. Sadow, I.I. Slowing, Direct 3D Printing of Catalytically Active Structures, ACS Catal. 7 (2017) 7567-7577.
[37] X. Sun, Y. Yan, L. Zhang, G. Ma, Y. Liu, Y. Yu, Q. An, S. Tao, Direct 3D Printing of Reactive Agitating Impellers for the Convenient Treatment of Various Pollutants in Water, Adv. Mater. Interf. 5 (2018).
[38] H. Lee, S.G. Lee, P.S. Doyle, Photopatterned oil-reservoir micromodels with tailored wetting properties, Lab on a Chip 15 (2015) 3047-3055.
[39] S. Yamabe, W. Guan, S. Sakaki, Three Competitive Transition States at the Glycosidic Bond of Sucrose in Its Acid-Catalyzed Hydrolysis, J. Org. Chem. 78 (2013) 2527-2533.
[40] R. Rinaldi, F. Schüth, Acid Hydrolysis of Cellulose as the Entry Point into Biorefinery Schemes, ChemSusChem 2 (2009) 1096-1107.
[41] G.W. Huber, A. Corma, Synergies between Bio- and Oil Refineries for the Production of Fuels from Biomass, Angew. Chem. Int. Ed. 46 (2007) 7184-7201.
[42] Y. Sun, J. Cheng, Hydrolysis of lignocellulosic materials for ethanol production: a review, Biores. Technol. 83 (2002) 1-11.
[43] Y.-H.P. Zhang, L.R. Lynd, Toward an aggregated understanding of enzymatic hydrolysis of cellulose: Noncomplexed cellulase systems, Biotechnol. Bioeng. 88 (2004) 797-824.
[44] F. Hammerer, L. Loots, J.-L. Do, J.P.D. Therien, C.W. Nickels, T. Friščić, K. Auclair, Solvent-Free Enzyme Activity: Quick, High-Yielding Mechanoenzymatic Hydrolysis of Cellulose into Glucose, Angew. Chem. Int. Ed. 57 (2018) 2621-2624.
[45] W. Chen, S. Enck, J.L. Price, D.L. Powers, E.T. Powers, C.-H. Wong, H.J. Dyson, J.W. Kelly, Structural and Energetic Basis of Carbohydrate–Aromatic Packing Interactions in Proteins, J. Am. Chem. Soc. 135 (2013) 9877-9884.
[46] A. Shrotri, H. Kobayashi, A. Fukuoka, Air Oxidation of Activated Carbon to Synthesize a Biomimetic Catalyst for Hydrolysis of Cellulose, ChemSusChem 9 (2016) 1299-1303.
[47] H. Kobayashi, M. Yabushita, T. Komanoya, K. Hara, I. Fujita, A. Fukuoka, High-Yielding One-Pot Synthesis of Glucose from Cellulose Using Simple Activated Carbons and Trace Hydrochloric Acid, ACS Catal. 3 (2013) 581-587.

[48] A.T. To, P.W. Chung, A. Katz, Weak‐Acid Sites Catalyze the Hydrolysis of Crystalline Cellulose to Glucose in Water: Importance of Post‐Synthetic Functionalization of the Carbon Surface, Angew. Chem. 127 (2015) 11202-11205.
[49] G.S. Foo, C. Sievers, Synergistic Effect between Defect Sites and Functional Groups on the Hydrolysis of Cellulose over Activated Carbon, ChemSusChem 8 (2015) 534-543.
[50] J. Dong, Y. Ozaki, K. Nakashima, Infrared, Raman, and Near-Infrared Spectroscopic Evidence for the Coexistence of Various Hydrogen-Bond Forms in Poly(acrylic acid), Macromolecules 30 (1997) 1111-1117.
[51] N.-S. Choi, Y.M. Lee, J.H. Park, J.-K. Park, Interfacial enhancement between lithium electrode and polymer electrolytes, J. Power Sources 119-121 (2003) 610-616.
[52] D. Singappuli-Arachchige, J.S. Manzano, L.M. Sherman, I.I. Slowing, Polarity Control at Interfaces: Quantifying Pseudo-solvent Effects in Nano-confined Systems, ChemPhysChem 17 (2016) 2982-2986.
[53] N. Sarkar, K. Das, D.N. Nath, K. Bhattacharyya, Twisted charge transfer processes of nile red in homogeneous solutions and in faujasite zeolite, Langmuir 10 (1994) 326-329.
[54] Z. Chen, H. Ji, C. Liu, W. Bing, Z. Wang, X. Qu, A Multinuclear Metal Complex Based DNase‐Mimetic Artificial Enzyme: Matrix Cleavage for Combating Bacterial Biofilms, Angew. Chem. Int. Ed. 55 (2016) 10732-10736.
[55] R. Bonomi, P. Scrimin, F. Mancin, Phosphate diesters cleavage mediated by Ce(iv) complexes self-assembled on gold nanoparticles, Org. Biomol. Chem. 8 (2010) 2622-2626.
[56] C.S. Yi, T.N. Zeczycki, S.V. Lindeman, Kinetic, Spectroscopic, and X-Ray Crystallographic Evidence for the Cooperative Mechanism of the Hydration of Nitriles Catalyzed by a Tetranuclear Ruthenium-μ-oxo-μ-hydroxo Complex, Organometallics 27 (2008) 2030-2035.
[57] C.S. Yi, T.N. Zeczycki, I.A. Guzei, Highly Cooperative Tetrametallic Ruthenium-μ-Oxo-μ-Hydroxo Catalyst for the Alcohol Oxidation Reaction, Organometallics 25 (2006) 1047-1051.
[58] M.F. Perutz, Mechanisms of cooperativity and allosteric regulation in proteins, Quart. Rev. Biophys. 22 (1989) 139-237.